Journal of Marine Science and Technology

Volume 26 | Issue 6 Article 4

HYDRODYNAMIC ANALYSIS OF UNDERWATER GLIDER WITH DIAMOND WING IN UNSTEADY AND NONUNIFORM FLOW FIELD

Chen-Wei Chen
Zhenjiang University, Ocean College, Zhoushan, China.

Zhuo Feng
Zhenjiang University, Ocean College, Zhoushan, China.

Xu Liang
Zhenjiang University, Ocean College, Zhoushan, China.

Recommended Citation

Chen, Chen-Wei; Feng, Zhuo; and Liang, Xu (2018) "HYDRODYNAMIC ANALYSIS OF UNDERWATER GLIDER WITH DIAMOND WING IN UNSTEADY AND NONUNIFORM FLOW FIELD," *Journal of Marine Science and Technology*: Vol. 26: Iss. 6, Article 4.
DOI: 10.6119/JMST.201812_26(6).0004
Available at: https://jmstt.ntou.edu.tw/journal/vol26/iss6/4

HYDRODYNAMIC ANALYSIS OF UNDERWATER GLIDER WITH DIAMOND WING IN UNSTEADY AND NONUNIFORM FLOW FIELD

Acknowledgements

We would like to thank the National Natural Science Foundation of China (No. 51409230) and Zhejiang Zhoushan Science and Technology Project (No. 2018C81041) and the National Key Special Research Plan of China Ministry of Education (No. 2017YFC0306100) for their financial support. In addition, we would like to thank Professor W. H. Wang at Zhejiang University and Taiwan Ocean University and the anonymous reviewers whose comments were helpful in improving the original manuscript.

Journal of Marine Science and Technology, Vol. 26, No. 6, pp. 787-802 (2018)
DOI: 10.6119/JMST.201812_26(6).0004

HYDRODYNAMIC ANALYSIS OF UNDERWATER GLIDER WITH DIAMOND WING IN UNSTEADY AND NONUNIFORM FLOW FIELD

Chen-Wei Chen, Zhuo Feng, and Xu Liang

Key words: computational fluid dynamics (CFD), hydrodynamic performance, underwater glider, nonuniform flow, unsteady flow, overlapping grid technology, Diamond-Wing, Sea-Wing.

ABSTRACT

In this study, the hydrodynamic performance of a proposed underwater glider (UG) that utilizes a diamond wing was analyzed and its gliding ability in undersea environments with both steady and uniform and unsteady and nonuniform oceanic currents optimized. The flow field around the UG was analyzed using the software package RANS CFD. Under conditions where the current varied linearly both with water depth and time, the UG exhibited harmonically heaving and pitching motions, with a constant acceleration incident flow. The dynamic lifting and drag forces acting on the diamond wing and the dynamic heaving force and pitching moment acting at the center-of-gravity of the UG body were also determined. The hull efficiency of the proposed Diamond-Wing UG showed an increase of 27%-45% for angles of attack (AOAs) in the range 2°-18° compared with the Sea-Wing UG, developed by the Shengyang Automatic Institution in 2013. Further, the lift-to-drag ratio of the wing increased by 6.5%-14% for AOAs in the range 4°-12°, and the optimal tilt angle for maximum hull efficiency and lift-to-drag ratio was found to be in the range 15°-20°. The results of comparison of the analysis algorithm and numerical model with the results of ellipsoids generated by theoretical calculations and calculations from various studies in the literature showed good agreement. The simulation results showed that the UG with the proposed diamond-shaped wing possesses anti-flow ability and strong maneuverability in nonuniform and unsteady inflow conditions.

I. INTRODUCTION

A conventional underwater glider (UG) is an autonomous underwater vehicle (AUV) with no external propulsion device. A UG mounted with a gliding wing is an energy-saving underwater observation platform that can be driven by buoyancy and gravity difference and the lifting force of the wing in the forward direction. The gliding performance of a UG depends predominantly on the hydrodynamic performance of the wing, including the anti-flow performance of the wing body in static, unsteady, uniform, and/or nonuniform flow fields. However, the low-speed of a conventional UG presents enormous problems when it operates in oceanic seas with strong currents that exceed its maximum forward speed, i.e., 1-2 knots. Thus, a novel hybrid-propulsion UG that combines the advantages of a buoyancy-driven UG and propeller-driven AUV has recently been proposed by Yang et al. (2016) to enhance service speed and maneuverability.

UGs are utilized extensively as important platforms in ocean exploration owing to their low cost and flexibility (Wang et al., 2011). They can carry a variety of practical marine monitoring sensors to obtain hydrologic data in oceanic seas, particularly in the vertical plane. Specifically, they can carry conductance temperature depth sensors to measure real-time parameters such as temperature, salinity, and depth, and provide key basic data for research in oceanography, marine meteorology, chemistry, and biology. In addition, different types of sensors can be mounted on UGs, such as portable oxygen concentration sensors, which can effectively monitor marine ecologies and support marine ecological protection and management (Graver and Leonard, 2001; Wu et al., 2010; Yu et al., 2011), and chlorophyll sensors, which can provide technical support for marine aquaculture and marine fishery development through monitoring of the parameters of phytoplankton in oceanic seas.

Optimization of the configuration of a UG, in which the hull is primarily combined with high-performance wings and appendages, has attracted considerable attention as a means of enhancing the performance of the sensors carried by the UG. For example, Jeans et al. (2010) utilized the structured grid to solve the Reynolds-averaged Navier-Stokes (RANS) equation in order to calculate the flow field characteristics of a slender body with a retraction tail. Holloway et al. (2015) studied flow separation from three slender revolution bodies in steady turning using computational fluid dynamics (CFD) RANS simulations. Wu et al. (2006) (Shenyang Institute of Automation, Chinese

Paper submitted 05/30/18; revised 08/08/18; accepted 10/26/18. Author for correspondence: Chen-Wei Chen (e-mail: cwchen@zju.edu.cn).
Zhenjiang University, Ocean College, Zhoushan, China.

Academy of Sciences) analyzed the hydrodynamic performance of a UG using the ANSYS-CFX CFD software, and the design of the main carrier, stabilizer wing, and lifting wing was optimized in the preliminary design of the Sea-Wing UG prototype.

Huang et al. (2010) (Naval Engineering University) calculated the hydrodynamic performance of the heaving and pitching motions of a submarine using the moving grid technology in the Fluent CFD code. Wu et al. (2008) adopted CFD to study the 3D viscous flow field around the SUBOFF submarine model. Ting et al. (2012) investigated the hydrodynamic performance of a UG using Fluent. Bettle et al. (2009) adopted the ANSYS-CFX viscous CFD solver to analyze the hydrodynamic performance of a 3000-T slender-body submarine. Furthermore, the results obtained by Bettle et al. (2009) were applied to model and simulate the motion of the submarine (Bettle et al., 2009; Chen et al., 2013a; Chen et al., 2013b; Bettle et al., 2014). Nevertheless, the flow field in actual oceanic seas is very complex; the hydrodynamic performance and motion behavior of a UG in nonuniform flow fields and/or unsteady flow fields are seldom studied.

Conventional UG prototypes as well as the well-known Sea-Wing UG (developed by the Shenyang Automatic Institution) are mounted with a traditional backswept wing (Yu et al., 2011; Yu et al., 2013). Since 2017, the record for the deepest diving depth achieved by UGs worldwide is more than 6000 m.

In this paper, a new UG fitted with a diamond-shaped wing and an X-type rudder is proposed based on the Sea-Wing Glider. The innovative diamond-shaped wing integrates a pair comprising a prepositive back-swept wing and a prepositive forward-swept wing with a higher height in heave than the prepositive one. NACA0012 is utilized for the wing profile and NACA0006 for the rudder section. A CFD Parametric Trade-off study on the configuration of the diamond wing was carried out to enhance hydrodynamic performance and improve the motion performance of the UG in both steady and uniform and nonuniform and unsteady oceanic currents. The study involved the following:

1. Analysis of CFD grid independence in order to select an appropriate time-saving grid number to estimate hydrodynamic force.
2. Verification of the CFD calculation results using experimental hydrodynamic coefficients of a slender ellipsoid with a slenderness ratio of 6:1, including inertial and damping hydrodynamic coefficients in heave and pitch motions. The numerical results were consistent with the experimental results. The verification was performed using viscous CFD solvers, STAR-CCM+, and ANSYS-CFX.
3. Estimation of the lift and drag forces of the UG mounted with a conventional sweepback wing (Sea-Wing UG) and the UG mounted with a diamond wing with variable tilt angles (5°-25°) (Diamond-Wing UG) using the angle of attack (AOA) and speeds for the optimal configuration of the UG.
4. Analysis of the hydrodynamic performance in pure-surging, oblique, and pure-heaving, and pure-pitching motions, using STAR-CCM+, overlapping grid technology, and user-defined functions (UDFs) to model and parameterize nonuniform and unsteady flow fields. Parametric studies on the heterogeneity of the nonuniform flow k_1 and acceleration of unsteady flow k_2 were also carried out to study the hydrodynamic behavior of the designed UG. The unsteady hydrodynamic performance was analyzed using the pure UG motion frequency, inflow heterogeneity, and strength.

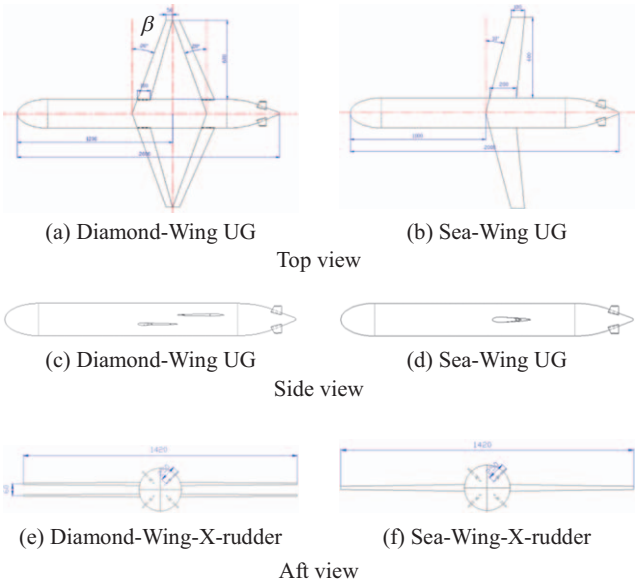

Fig. 1. Schematic structure of the Diamond-Wing and Sea-Wing UGs mounted with X-type rudder.

The remainder of this paper is organized as follows. Section 2 describes the proposed Diamond-Wing UG design and related parameters. Section 3 presents the corresponding formulation of CFD processing and boundary condition. Section 4 outlines the process of verification of the CFD study. Section 5 describes the configuration trade-off study conducted on the proposed UG and compares the simulation results of two types UGs. Finally, Section 6 presents concluding remarks and discussion.

II. UNDERWATER GLIDER DESIGN AND RELATED PARAMETERS

1. Design of the Proposed UG

The proposed UG comprises three major parts, shown in Figs. 1(a), (c), and (e). The main body of the UG has a torpedo-type hull, Figs. 1(a) and (b). Tilt angle β is shown in Fig. 1(a), which is the intersection angle of the forward-swept wings and the cross section of main body. The UG has a diamond-shaped wing comprising a set of forward-swept wings and a set of back-swept wings, both of which have an elevation difference. The four wings are doubly symmetrical in the top view of the UG geometry, as shown in Fig. 1(a). The third part is the X-type rudder, arranged as shown in Fig. 1(c). The NACA 0006 pro-

Table 1. Definition of kinematic and kinetic parameters of UG.

DOF			Forces/Moments	Linear/Angular Vel.	Position/Euler angles
1	Motion in the X-direction	(surge)	X	u	ξ
2	Motion in the Y-direction	(sway)	Y	v	η
3	Motion in the Z-direction	(heave)	Z	w	ζ
4	Rotation about the X-axis	(roll)	K	p	φ
5	Rotation about the Y-axis	(pitch)	M	q	θ
6	Rotation about the Z-axis	(yaw)	N	r	ψ

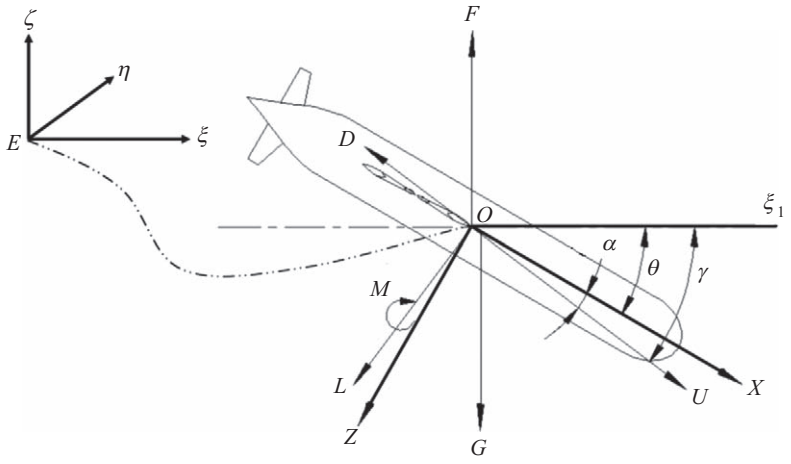

Fig. 2. Coordinate system and definition of hydrodynamic forces, moments, and angles.

file is used for the tail stabilizer, and the NACA 0012 profile for the wing sections, owing to their high lift coefficients. The novelty of the design is the wing arrangement. The three-view drawing of the conventional contrastive UG, namely Sea-Wing, is shown in Figs. 1(b), (d), and (f).

The merit of the design in Figs. 1(a), (c), and (e) is that the hydrodynamic interaction performance between the forward-swept and back-swept wings can be enhanced by parametric research in CFD. The basic principle is that the high flow velocity on the suction side of the prepositive wing can enhance the flow velocity on the pressure side of the postpositive wing. Simultaneously, the effect of the Diamond-Wing tilt angle on the enhanced flow velocity on the pressure side of the postpositive wing is significant as it enhances the wing-body lift-to-drag ratio and the UG's motion performance.

2. Analysis Parameters

The most important parameters considered in the analyses are the tilt angle (β) and aspect ratio (AR) of the diamond-shaped wing. The AR of the diamond-shaped wing is defined as the ratio of the length of the long diagonal to the short diagonal. Thus, the congruent relationship between the tilt angle and aspect ratio (β, AR) has (5°, 11.3), (10°, 5.67), (15°, 3.69), (20°, 2.57), (25°, 2.14) in this study.

When analyzing UG motion with six degrees of freedom (6-DOF), it is convenient to define two coordinate frames. A translation-rotating coordinate frame O-XYZ fixed on the UG is called the body-fixed coordinate frame, described as a non-inertial reference frame. The other is an Earth-fixed reference frame E-$\xi\eta\zeta$ that can be considered as an inertial frame to study steady and unsteady flow fields. During steady gliding, the UG is affected by fluid dynamic forces and moments as well as weight and buoyancy. Under stable gliding conditions, the sum of these forces is zero. Force analysis and parameter definitions of hydrodynamic forces, moments, and angles are shown in Fig. 2—where γ is the gliding angle, α is the AOA, θ is the pitch angle, G is gravity, L is the lift force, F is the buoyancy, D is the resistance, and M is the hydrodynamic pitch moment.

The triple velocity and triple angular velocity of the UG with 6-DOF are represented by u, v, w, p, q, r, respectively; the 6-DOF triple acceleration and triple angular acceleration are denoted by $\dot{u}, \dot{v}, \dot{w}, \dot{p}, \dot{q}, \dot{r}$, respectively; and the triple force and triple moment are represented by X, Y, Z, K, M, N. The relevant kinematic and kinetic parameters are defined in Table 1.

Fig. 3 shows the configuration design process integrated with the hydrodynamic performance estimation in this study.

The hydrodynamic performance of the two UGs, as shown in Fig. 4, was compared on the basis of the same wetted areas of the total wing-body combinations.

III. CFD PROCESSING AND BOUNDARY CONDITIONS

1. Governing Equation

The Navier-Stokes governing equation was used to calculate

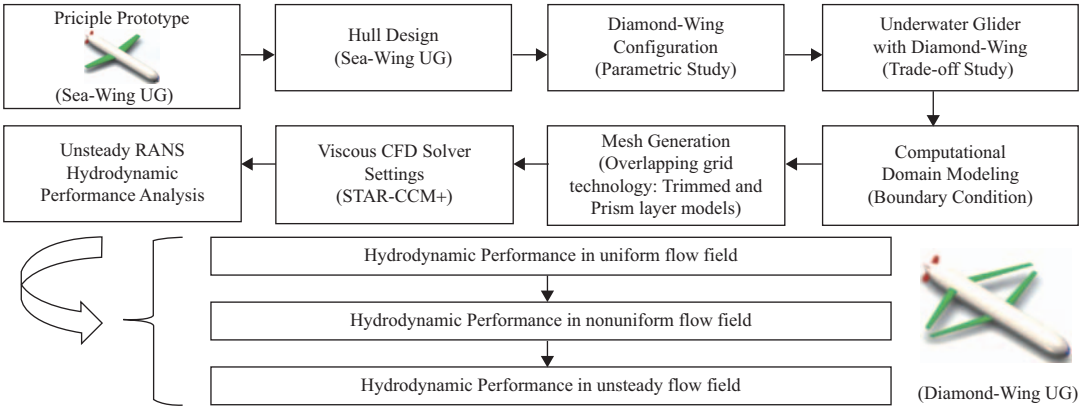

Fig. 3. Design process of Diamond-Wing UG based on Sea-Wing UG.

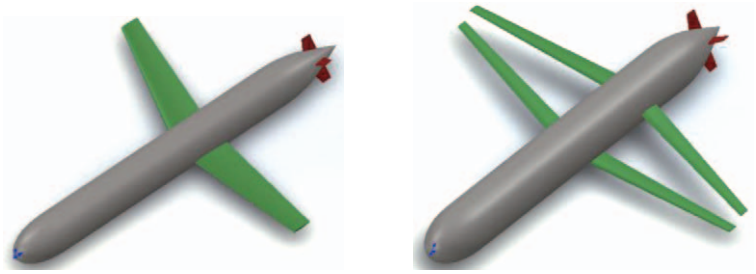

(a) Sea-Wing UG (b) Diamond-Wing UG

Fig. 4. Comparison of two types of UGs: (a) UG mounted with conventional backswept wing; (b) UG mounted with diamond wing.

the stress and velocity distribution on the surface of the Diamond-Wing UG, thus obtaining the lift, drag, and moment, described as follows (Liu et al., 2016):

$$\frac{\partial\left(\overline{u_i}\right)}{\partial u_i}=0 \text{ and} \tag{1}$$

$$\frac{\partial\left(\rho\overline{u_i}\right)}{\partial t}+\rho\overline{u_j}\frac{\partial\overline{u_i}}{\partial x_j}=\rho\overline{F_i}-\frac{\partial\overline{P}}{\partial x_i}+\frac{\partial}{\partial x_j}\left(\mu\frac{\partial\overline{u_i}}{\partial x_j}-\rho\overline{u_i'u_j'}\right), \tag{2}$$

where u_i is the component of the average speed, u_i' is the turbulent pulsation velocity component relative to the hourly average flow velocity, $\overline{F_i}$ is the component of the mass force, $\overline{P}$ is the pressure, μ is the dynamic viscosity coefficient of a fluid, and $\rho\overline{u_i'u_j'}$ is the Reynolds average stress.

The grid type was different when using the two CFD solvers, STAR-CCM+ and ANSYS-CFX; however, both solvers adopted the k-ε turbulence model and the same parameters. Turbulent kinetic energy k and turbulent dissipation rate ε are defined as follows (Sakthivel et al., 2011):

$$k=\frac{\overline{u_i'u_j'}}{2}=\frac{1}{2}\left(\overline{u'^2}+\overline{v'^2}+\overline{w'^2}\right) \text{ and} \tag{3}$$

$$\varepsilon=\frac{u}{\rho}\overline{\left(\frac{\partial u_j'}{\partial x_k}\right)\left(\frac{\partial u_i'}{\partial x_k}\right)}. \tag{4}$$

Turbulent viscosity μ_t is a function of k and ε:

$$\mu_t=\rho C_\mu\frac{k^2}{\varepsilon}, \tag{5}$$

where C_μ is an empirical constant; C_μ = 0.09. In the standard k-ε model, the corresponding transport equation is

$$\begin{cases}\dfrac{\partial(\rho k)}{\partial t}+\dfrac{\partial(\rho k u_i)}{\partial x_i}=\dfrac{\partial}{\partial x_j}\left[\left(\mu+\dfrac{u_i}{\sigma_k}\right)\dfrac{\partial k}{\partial x_j}\right] \\ \qquad\qquad +G_k+G_b-\rho\varepsilon-Y_M+S_k \\ \dfrac{\partial(\rho\varepsilon)}{\partial t}+\dfrac{\partial(\rho\varepsilon u_i)}{\partial x_i}=\dfrac{\partial}{\partial x_j}\left[\left(\mu+\dfrac{u_i}{\sigma_\varepsilon}\right)\dfrac{\partial\varepsilon}{\partial x_j}\right] \\ \qquad\qquad +C_{1\varepsilon}\dfrac{\varepsilon}{k}(G_k+C_{3\varepsilon}G_b)-C_{2\varepsilon}\rho\dfrac{\varepsilon^2}{k}+S_\varepsilon\end{cases}, \tag{6}$$

where G_k is the generation of turbulent kinetic energy k caused by the average speed gradient; G_b is the generation of turbulent kinetic energy k caused by buoyancy; Y_M denotes the contribution of pulsatile expansion in compressible turbulence; $C_{1\varepsilon}$, $C_{2\varepsilon}$,

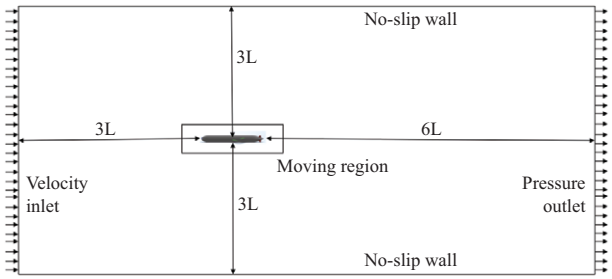

Fig. 5. Computational domain and boundary conditions.

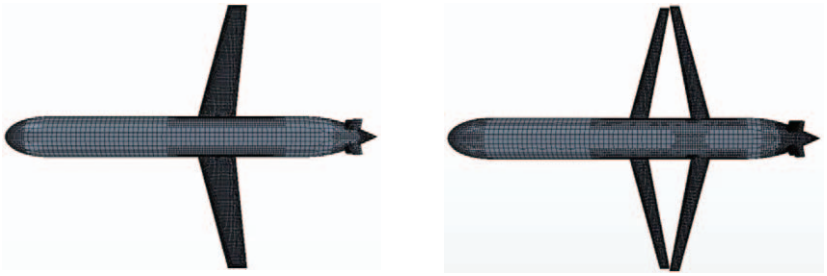

(a) Conventional UG (b) Diamond-Wing UG

Fig. 6. Mesh generated around UGs.

and $C_{3\varepsilon}$ are empirical constants; σ_k and σ_ε are the Prandtl numbers corresponding to turbulent kinetic energy k and dissipation rate ε, respectively; S_k and S_ε are user-defined source items.

2. Computational Domain and Grid Generation

Fig. 5 shows the designed computational domain and boundary conditions. The Diamond-Wing UG has a length of 2.0 m, width of 1.4 m, and a maximum diameter of 0.22 m. The coordinates of the origin are arranged at the middle of the model, the background area is rectangular, measuring 21.0 m × 6.0 m × 12.0 m; the moving region, also rectangular, measures 0 m × 2.0 m × 1.0 m; the velocity inlet is located 6.0 m upstream of the calculation model's bow, and the pressure outlet is in the calculation model's stern, located 12.0 m downstream.

In Fig. 5, overlapping grid technology, including a trimmed mesher model and a prism layer mesher model, was applied to generate static and dynamic grids. The technology of the surface remesher model in STAR-CCM+ was applied to mesh the surfaces of UGs. Hexahedral grids were generated using the cutting-body grid generator and the minimum number of grids on the main wing and empennage were 2×10^{-4} m. Further, five layers of prismatic boundary-layer grids were produced to satisfy the requirements of the distribution of value Y+, as shown in Fig. 6. The Y+ value in this study was set to 30-300, the number of boundary layers was five, the growth rate of the boundary layers was 1.2, and the thickness of the first boundary layer Δy was derived using Eq. (7) (Chen et al., 2017):

$$\Delta y = L y^{+} \sqrt{80}\, \mathrm{Re}^{-\frac{13}{14}}, \qquad (7)$$

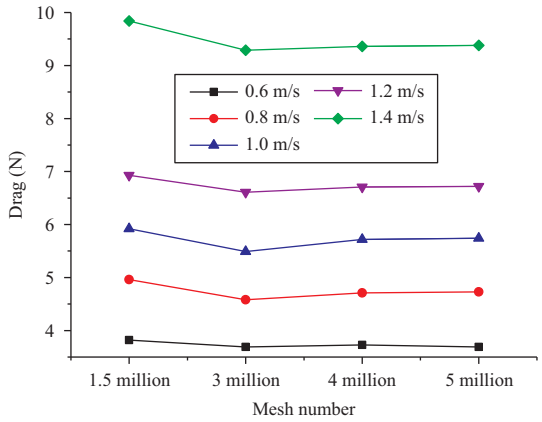

Fig.7. Variations of grid number versus drag force and velocities from 0.6 to 1.4 m/s.

where L is UG length, Re is Reynolds number and $\mathrm{Re} = VL/\upsilon$, and V is inlet velocity; the ambient temperature was 17°C in this numerical simulation, and the corresponding kinematic viscosity was $\upsilon = 1.08 \times 10^{-6}$.

The number of grids is the key factor affecting the computational accuracy and time, i.e., grid-independent study. In this study, the drag performance in straight-line motion with different inlet velocities from 0.6 to 1.4 m/s was calculated using 5×10^6, 4×10^6, 3×10^6, and 1.5×10^6 grids, as shown in Fig. 7. The results show that as the number of grids approaches 4×10^6, the drag forces converge to a certain value, whereas the numbers of grids continue to increase. Thus, 4×10^6 grids were used to calculate the UGs' hydrodynamic performance for enhanced computational efficiency.

Fig. 8. Geometric model of ellipsoid.

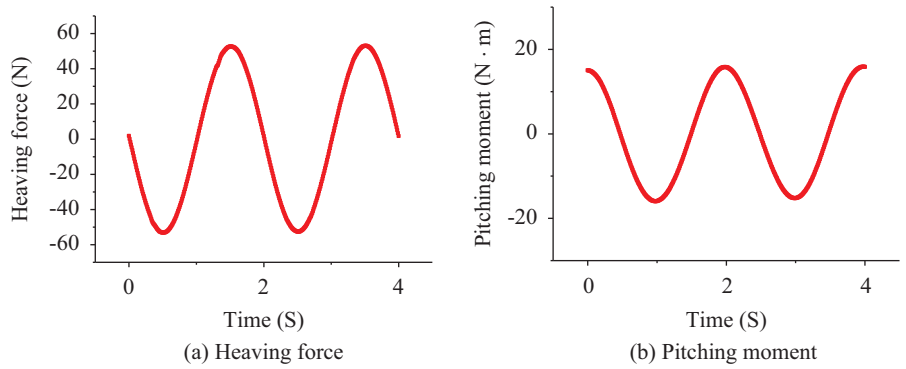

Fig. 9. Hydrodynamic performance of the ellipsoid constrained in pure heaving motion.

IV. VERIFICATION OF HYDRODYNAMIC PERFORMANCE

1. Verification Using an Ellipsoid with Slenderness Ratio of 6:1

An ellipsoid model with a slenderness ratio of 6:1 was selected to verify the accuracy of the calculation method in this study and compared with the experimental and reference values. The cross section of the ellipsoid is a circle with $r = 0.25$ m and the long axis $a = 1.5$ m. The geometric model is shown in Fig. 8.

Computational domain creation and grid partitioning were performed using the procedure given in Section 3.2. The pure heaving motion of the ellipsoid in a steady uniform flow field is defined as follows:

$$\begin{cases} \zeta = 0.015\sin \pi t \\ \theta = \dot{\theta} = 0 \\ w = \dot{\zeta} = 0.015\pi \cos \pi t \\ \dot{w} = -0.015\pi^2 \sin \pi t \end{cases} \tag{8}$$

The heaving force and pitching moment were obtained using a viscous CFD solver (STAR-CCM+) while the ellipsoid was constrained in the pure heaving motion. The calculation time step was 0.01 s. Fig. 9 shows the scatter data of the ellipsoidal heaving forces and pitching moments. The pure ellipsoidal heaving motion and pitching motion performed stable oscillation for 4.0 s.

The pure heaving motion is defined as:

$$\begin{cases} \xi = a\sin \omega t \\ \theta = \dot{\theta} = 0 \\ w = \dot{\xi} = a\omega \cos \omega t \\ \dot{w} = -a\omega^2 \sin \omega t \end{cases} \tag{9}$$

The heave forces Z affected by heave velocity w and heave acceleration $\dot{w}$ were denoted as Z_w and $Z_{\dot{w}}$, respectively. The pitch moments M affected by heave velocity w and heave acceleration $\dot{w}$ were denoted as M_w and $M_{\dot{w}}$, respectively. Taking advance of Fourier series expansion, Z and M can be formulated as:

$$\begin{cases} Z = Z_{\dot{w}}\dot{w} + Z_w w + Z_0 \\ \quad = -a\omega^2 Z_{\dot{w}} \sin \omega t + a\omega Z_w \cos \omega t + Z_0 \\ M = M_{\dot{w}}\dot{w} + M_w w + M_0 \\ \quad = -a\omega^2 M_{\dot{w}} \sin \omega t + a\omega M_w \cos \omega t + M_0 \end{cases}. \tag{10}$$

The corresponding dimensionless formulation and coefficients were denote as following:

$$\begin{cases} Z' = Z_a \sin \omega t + Z_b \cos \omega t + Z_0 \\ M' = M_a \sin \omega t + M_b \cos \omega t + M_0 \end{cases}, \text{ and}$$

$$\begin{aligned} Z_a &= -\frac{aw^2 L}{V^2} Z_{\dot{w}}'; \; Z_b = -\frac{aw}{V} Z_w'; \\ M_a &= -\frac{aw^2 L}{V^2} M_{\dot{w}}'; \; M_b = -\frac{aw}{V} M_w'. \end{aligned} \tag{11}$$

Table 2. Validation and comparison of hydrodynamic derivatives in heave and pitch motions.

	$Z'_{\dot{w}}$	Z'_{w}	$M'_{\dot{w}}$	M'_{w}
Present study	-0.0265	-0.0086	0.00007	0.0246
Theoretical data	-0.0271	*Null*	0.00000	*Null*
Zhang, et al., 2016	-0.0261	-0.0090	*Null*	0.0222
Zhang, et al., 2008	-0.0282	-0.0237	0.00002	0.0258
Yang, et al., 2009	-0.0255	-0.0227	*Null*	0.0240
Huang, et al., 2008	-0.0271	-0.1080	0.00003	0.0234

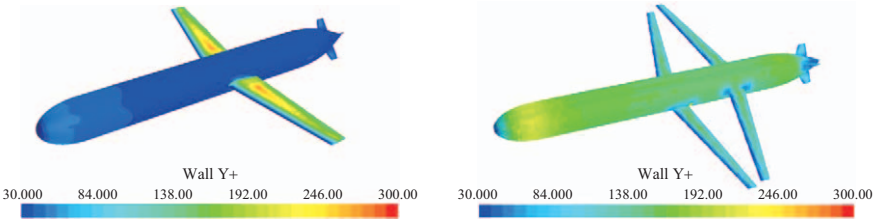

(a) Sea-Wing UG (b) Diamond-Wing UG

Fig. 10. y+ value on the UGs.

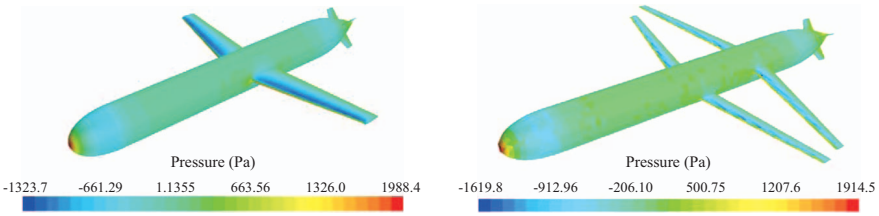

(a) Sea-Wing UG (b) Diamond-Wing UG

Fig. 11. Pressure distribution on the UGs in straight-line motion with velocity of 2.0 m/s.

After importing the discrete point data into MATLAB, the hydrodynamic derivatives were calculated through fitting and normalization. Table 2 compares the calculation results, experimental values, and values available in the literature. The numerical simulation results obtained in this study are in good agreement with the theoretical data and calculation results available in the literature (Huang et al., 2008; Zhang et al., 2008; Yang et al., 2009; Zhang et al., 2016), which verifies the reliability of the research method presented in this paper. In particular, the comparison results of dimensionless derivatives $Z'_{\dot{w}}$ and M'_{w} are in good agreement.

2. Verification Using Viscous CFD Solvers

To verify the accuracy of the calculations, the hydrodynamic performance of the Diamond-Wing UG and Sea-Wing UG in straight-line and oblique motions in steady uniform flow was analyzed using both STAR-CCM+ and ANSYS-CFX CFD solvers with the grid settings and physical model described in the previous section. Figs. 10(a) and (b) show that the y+ value, i.e., a local Reynolds number, on the UGs is entirely between 30 and 300, which guarantees the accuracy of the calculation results.

Figs. 11(a) and (b) show that the pressure distribution on the surface of the Sea-Wing UG and the Diamond-Wing UG was in straight-line motion with a velocity of 2.0 m/s. The pressure distributions on the Sea-Wing UG and the Diamond-Wing UG differ because the Diamond-Wing configuration changes the hydrodynamic interference between the backswept and forward-swept wings

Fig. 12 shows the validation results, the variation of the lift and drag forces versus the AOA of the Diamond-Wing UG in a uniform flow field. The results were estimated by using STAR-CCM+ and ANSYS-CFX CFD solvers modeled with different grid type and numbers (Table 3). Nevertheless, they are consistent and within the margin of tolerance, ensuring the accuracy of the calculation results. When the attack angle approaches 4°, the lift-to-drag ratio is the largest. The maximum value of the lift is approximately 16°; when the attack angle is greater than 16°, both the lift force decreases, i.e., stall phenomenon.

3. Computer Simulation

The hydrodynamic performance of the Diamond-Wing UG was determined based on the overlapping grid technology in the fluid simulation software STAR-CCM+ together with hexahedral

Table 3. Computational Parameters.

Parameter	STAR-CCM+	ANSYS-CFX
Computing	4*Intel Xeon CPU, 72 Core, 36 Thread, 2.1 GHz, 256 GB of RAM	4*Intel Xeon CPU, 72 Core, 36 Thread, 2.1 GHz, 256 GB of RAM
No. of elements	4.0 million	2.0 million
Grid type	Hexahedral grids	Unstructured grids
Turbulence model	k-ε	k-ε
Convergence control	residual < 10^{-4}	residual < 10^{-5}

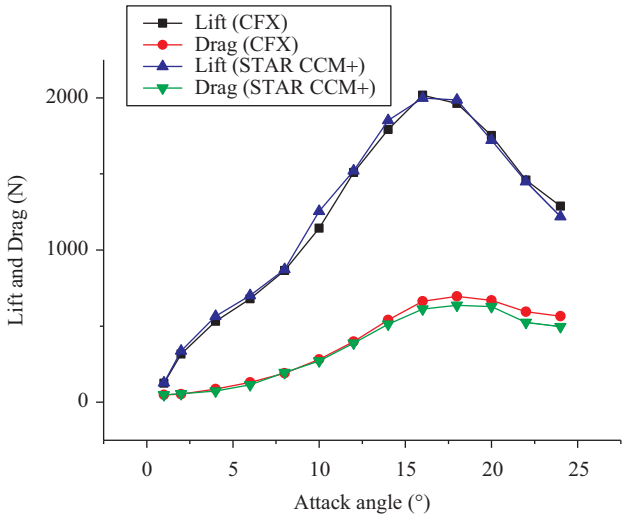

Fig. 12. Validation study: lift and drag of Diamond-Wing UG in oblique motion in steady and uniform flow field with velocity of 2.0 m/s.

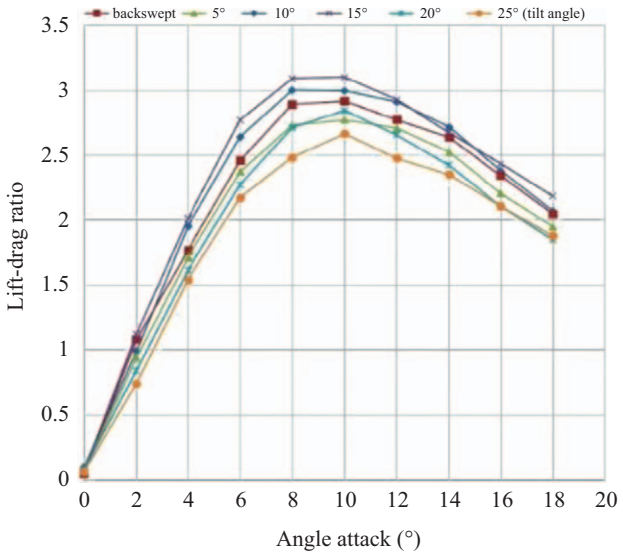

Fig. 13. Variations of lift-to-drag ratio with respect to angle of attack with different diamond-shaped hydrofoil tilt angles (5° to 25°) and conventional backswept wing.

grid model (4 million elements) and compared with the simulation results obtained using the commercial finite volume code ANSYS-CFX together with unstructured grid model (2 million elements). The ANSYS-CFX and STAR-CCM+ simulation results were calculated using the high-resolution advection scheme. The residual type was set to root mean square (RMS), and the residual target was set to 1×10^{-5} for the ANSYS-CFX results and 1×10^{-4} for the STAR-CCM+ results. Table 3 gives the computational parameters applied in this CFD study.

V. CONFIGURATION TRADE-OFF STUDY AND SIMULATION RESULTS

1. UG Configuration Design in Steady Uniform Flow

Various diamond-shaped hydrofoil tilt angles (5° to 25°) of UGs were obtained, i.e., various Diamond-Wing aspect ratios. Using the adaptive grid technology, lift and drag forces were calculated under different angles of attack in the vertical plane while gliding at a velocity of 0.5 m/s. The variations of lift-to-drag ratio with respect to the attack and tilt angles are shown in Fig. 13. The simulation results showed that the designed Diamond-Wing UG mounted with a tilt angle of 15° gave a hydrodynamic performance better than that of the conventional backswept wing and other wing types.

The effective horsepower (*EHP*) of the diamond-wing UG and conventional UG at different angles of attack can be obtained using the glider resistance curve (Kannappa et al., 2015):

$$EHP = D \times v \,, \tag{12}$$

where *EHP* is the effective propulsion horsepower generated by the hull form and diamond-shaped wings, D is the total resistance of the hull with the wing appendage, and v is the UG gliding speed in surge. In this study, the thrust horsepower (*THP*) produced by the diamond-shaped wing can be expressed as follows:

$$THP = L \times \sin\alpha \times v + T \times v_a \,, \tag{13}$$

where *THP* is the thrust horsepower generated by the diamond-shaped hydrofoils in surge, L is the lift force, α is the AOA, v is the gliding speed of UG, T is the thrust, and v_a is the speed of advance of the glider. The term $T \times v_a$ is ignored in this study and shall be taken into account when the UG is mounted with hybrid propulsion, e.g., propellers and/or buoyancy engines.

The *EHP* and *THP* curves illustrated in Fig. 14 show that the *EHP* of the UG with a diamond-shaped wing at tilt angles of 15°, 20°, and 25° was less than that of the conventional UG. In addition, the *THP* of the diamond-wing UG at tilt angles of

Table 4. Comparison of the hull efficiency of the Diamond-Wing and Sea-Wing UGs at different AOA.

AOA (°)	Hull Efficiency			
	Diamond-Wing			Sea-Wing
	$\beta = 15°$	$\beta = 20°$	$\beta = 25°$	Backswept
	(1)	(2)	(3)	(4)
2	1.09562	0.84907	0.75181	0.8
4	1.10351	0.84907	0.74868	0.78
6	1.10351	0.84907	0.75719	0.77
8	1.10351	0.83062	0.75719	0.76
10	1.15366	0.84907	0.74036	0.75
12	1.26699	0.84907	0.64902	0.7
14	1.24589	0.86299	0.60774	0.68
16	1.13144	0.85996	0.7476	0.77
18	1.23808	0.84907	0.66763	0.7

Table 5. Comparison of the hull efficiency of the Diamond-Wing UGs different from the Sea-Wing UG.

AOA (°)	Hull Efficiency Difference		
	Diamond-Wing tilt angle		
	$\beta = 15°$	$\beta = 20°$	$\beta = 25°$
	$\frac{(1)-(4)}{(1)} *100$ (%)	$\frac{(2)-(4)}{(2)} *100$ (%)	$\frac{(3)-(4)}{(3)} *100$ (%)
2	26.98	5.78	-6.41
4	29.32	8.13	-4.18
6	30.22	9.31	-1.69
8	31.13	8.50	-0.37
10	34.99	11.67	-1.30
12	44.75	17.56	-7.85
14	45.42	21.20	-11.88
16	31.95	10.46	-2.99
18	43.46	17.56	-4.84

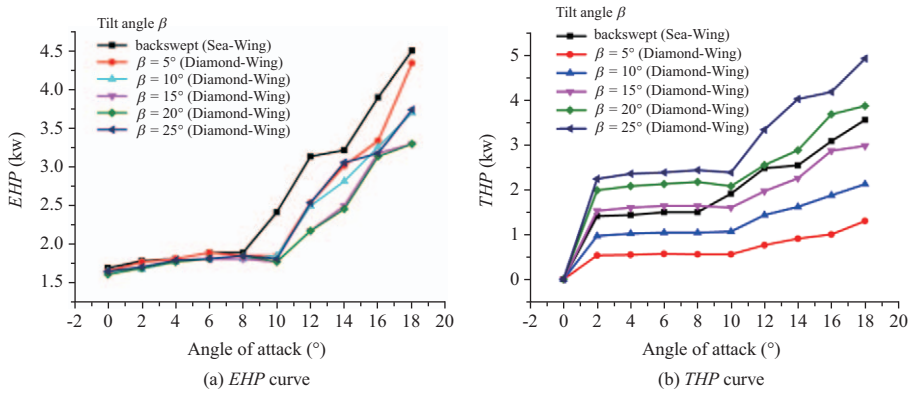

Fig. 14. Variations of *EHP* and *THP* with respect to AOA.

20° and 25° was also less than that of the conventional backswept-wing UG. When gliding, energy consumption is proportional to *EHP* and *THP*. Thus, the diamond-shaped wing glider design had lower power consumption characteristics.

The hull efficiency of the UGs with different wing configurations can be defined as the ratio of *EHP* (Eq. (12)) to *THP* (Eq. (13)) to analyze the performance of the design; thus, the hull efficiency can be expressed as

$$\eta = EHP / THP . \quad (14)$$

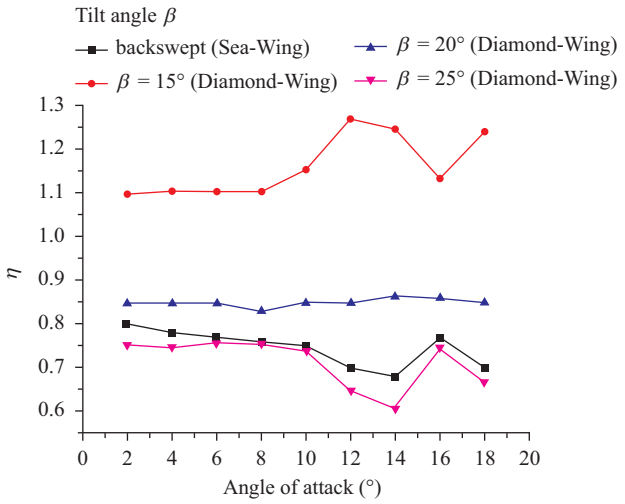

Fig. 15. Effect of Diamond-Wing tilt angle (aspect ratio) on hull efficiency.

The effective powers of the diamond-wing UG at tilt angles β of 15°, 20°, and 25° and the conventional backswept wing UG are shown in Fig. 15. Based on the same wetted surface, the UG with Diamond-Wing tilt angles β of 15° and 20° has higher hull efficiency than the UG with the traditional backswept hydrofoil. It is worth mentioning that for variations in terms of hull efficiency with respect to AOA in the range 10°-16°, the UG mounted with a Diamond-Wing β of 15° enhances the hull efficiency locally whereas that of the Sea-Wing and Diamond-Wing β of 25° considerably reduces it. Simulation results show that the designed UG configuration with a Diamond-Wing tilt angle of 15° has an enhanced hull efficiency greater than one, and greater than other cases at a speed of 1.0 knots. In addition, the UG mounted with a Diamond-Wing β of 20° has a relatively smooth trend in the variation of hull efficiency with respect to the AOA. The effect of Diamond-Wing tilt angle β on hull efficiency relative to that of the backswept Sea-Wing UG at AOAs of 2°-18° was also analyzed, the comparison results are presented in Tables 4 and 5.

The phenomenon shown in Fig. 15 can be explained. The proposed Diamond Wing integrated with a prepositive backswept wing and postpositive forward-swept wing have a higher altitude in heave than the prepositive wing. Hence, the high flow velocity on the suction side of the prepositive wing enhances the flow velocity on the pressure side of the postpositive wing. Simultaneously, the effect of the Diamond-Wing tilt angle on the enhanced flow velocity on the pressure side of the postpositive wing is significant. Consequently, this phenomenon presents two major results: (1) the hull efficiency of the UG with a Diamond-Wing tilt angle of 15° increases by 27% to 45% for AOAs of 2°-18°, and (2) the lift-to-drag ratio of the wing increases by 6.5% to 14% for AOAs of 4°-12°, as shown in Fig. 15. The comparisons were made on the basis that the motion of the UG body and the projected area of wing are the same. However, the Diamond-Wing interdependent interference of the prepositive backswept wing and a postpositive forward-swept wing is very complex. An interesting phenomenon in this study is that a Diamond-Wing tilt angle of 15° produces better hull efficiency than that of a Sea-Wing and Diamond-Wing tilt angle of 25° in which the AOA is in the range of 8°-16°.

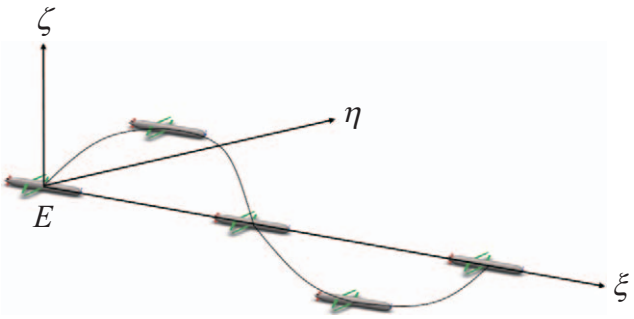

Fig. 16. Schematic of pure heaving motion.

In conclusion, (1) a Diamond-Wing tilt angle of 20° is a critical point for enhancing or reducing the hull efficiency in this Diamond-Wing UG configuration design with a service speed of 1 knot in a steady uniform flow field. (2) these simulation results show that the proposed Diamond-Wing configuration design is of considerable significance to parametric study on the Diamond-Wing hydrodynamic optimization for enhanced UG motion performance in steady uniform and/or unsteady nonuniform flow, as shown in the following sections.

2. Hydrodynamic Performance of Forced-Kinematic-State UG in Nonuniform Steady Flow

Extending the optimization design discussed in section 5.1, the motion performance of the Diamond-Wing UG (tilt angle β = 15°) during heave and pitch motions in a nonuniform flow field is analyzed in this section (the motion performance of the Diamond-Wing UG (tilt angle β = 15°) during heave and pitch motions in an unsteady flow field is discussed in section 5.3). The initial condition of the flow and forced kinematic state of the UG in the four cases studied are presented in Table 6.

The initial condition of nonuniform steady flow and forced UG motion in heave is shown in Case 1 in Table 6. The schematic shown in Fig. 16 illustrates that the UG performs a pure heaving motion; the kinematic equation is modeled as follows:

$$\begin{cases} \zeta = a\sin\omega t \\ \theta = \dot{\theta} = 0 \\ w = \dot{\zeta} = a\omega\cos\omega t \\ \dot{w} = -a\omega^2\sin\omega t \end{cases} \tag{15}$$

where ζ is the UG displacement along the ζ-axis; a is the amplitude of the heaving motion (a = 0.05 in this study); ω is the circular frequency of the heaving motion; θ is the pitch angle; w is the UG's heave velocity along the ζ-axis.

Table 6. Initial condition of flow and forced UG kinematic state.

Case Study	Flow Condition	Forced UG body motion					
		Heave		Pitch		Surge	
Case 1	Nonuniform Steady	Displacement	$a\sin\omega t$	Displacement	0	Displacement	$U_1 t$
		Velovity	$a\omega\cos\omega t$	Velovity	0	Velovity	U_1
		Accelaration	$-a\omega^2\sin\omega t$	Accelaration	0	Accelaration	0
Case 2	Nonuniform Steady	Displacement	0	Displacement	$\theta_0\sin\omega t$	Displacement	$U_1 t$
		Velovity	0	Velovity	$\theta_0\omega\cos\omega t$	Velovity	U_1
		Accelaration	0	Accelaration	$-\theta_0\omega^2\sin\omega t$	Accelaration	0
Case 3	Nonuniform Unsteady	Displacement	$a\sin\omega t$	Displacement	0	Displacement	$U_2 t$
		Velovity	$a\omega\cos\omega t$	Velovity	0	Velovity	U_2
		Accelaration	$-a\omega^2\sin\omega t$	Accelaration	0	Accelaration	k_2
Case 4	Nonuniform Unsteady	Displacement	0	Displacement	$\theta_0\sin\omega t$	Displacement	$U_2 t$
		Velovity	0	Velovity	$\theta_0\omega\cos\omega t$	Velovity	U_2
		Accelaration	0	Accelaration	$-\theta_0\omega^2\sin\omega t$	Accelaration	k_2

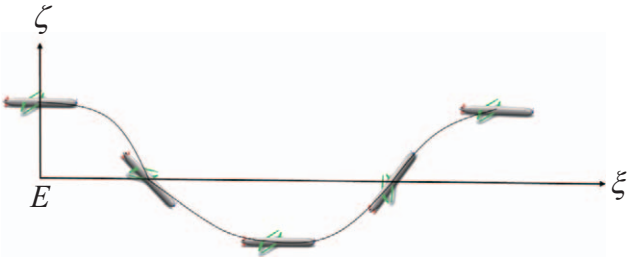

Fig. 17. Schematic of pure pitching motion.

Fig. 17 shows the schematic of a pure pitching motion performed by the UG. The kinematic equation is defined as follows:

$$\begin{cases} \theta = \theta_0 \sin\omega t \\ q = \dot{\theta} = \theta_0 \omega \cos\omega t \\ \dot{q} = -\theta_0 \omega^2 \sin\omega t \\ w = \dot{w} = 0 \end{cases}, \tag{16}$$

where θ is the pitch angle (θ_0 = 0.1 rad in this study); q is the UG angular velocity around the y- axis; ω is the circular frequency of the pitching motion; w is the UG's heave velocity along the ζ-axis. Table 6 gives the kinematic parameters for the heaving and pitching motions.

The low-speed capability presents enormous problems when a UG operates in strong currents that exceed the maximum forward speed of the UG. Therefore, we performed motion simulation of this special UG in strong current conditions with a speed of approximately 2.0 m/s. The nonuniform flow field was linearly distributed along the ζ-axis direction, i.e., in depth. This was formulized and generated with the UDF in the STAR-CCM+ solver as (Yu et al., 2015)：

$$U_1 = U_0 + k_1 \times z, \tag{17}$$

where U_1 is the velocity of nonuniform flow; U_0 is the initial velocity (= 2.0 m/s); k_1 denotes the heterogeneity of nonuniform flow (= 0.1, 0.3, and 0.5); z denotes the depth variation in the ζ-axis (Fig. 17).

The circular frequency of heaving motion ω was set at 10π. The frequency of the heaving motion f was 5 Hz, the nonuniform inlet velocity was set using the UDF according to Eq. (17). The time step was taken as 0.001 s in the following simulations. Fig. 18(a) show that the heaving force of the Diamond-Wing UG performed pure heaving motion in a nonuniform flow field in terms of time history. Figs. 18(b) and (c) show that the heaving force and pitching moment of the Diamond-Wing UG performed pure pitching motion in a nonuniform flow field in terms of time history, respectively. The heaving force and pitching moment exerted on the UG are seen to increase with an increase in the motion frequency. However, the linear distribution of the flow velocity along the ζ-axis causes the asymmetric trend of heaving force in time history. Hence, the absolute value of the peak of the entire heaving force curve and pitching moment curve are slightly higher than the absolute value of the trough.

Fig. 18 shows that the variation in inflow nonuniformity k_1 has some influence on the hydrodynamic performance. With the increase in k_1, the trend of change of heaving force and pitching moment also shift upward and is most obvious at the peak value. According to Yu et al. (2015), the effect of nonuniform flow on the pitching moment is most obvious; the resulting waveform curve near the wave trough is not smooth, but the concave part appears, and the peak value is significantly higher than the trough value (Yu et al., 2015). Although the nonuniformity coefficient k_1 changes, the heaving force and pitching moment exerted on this Diamond-Wing UG did not change significantly. In conclusion, this UG possesses good anti-flow performance.

3. Hydrodynamic Performance in Nonuniform and Unsteady Flow Field

The hydrodynamic performance of the Diamond-Wing UG

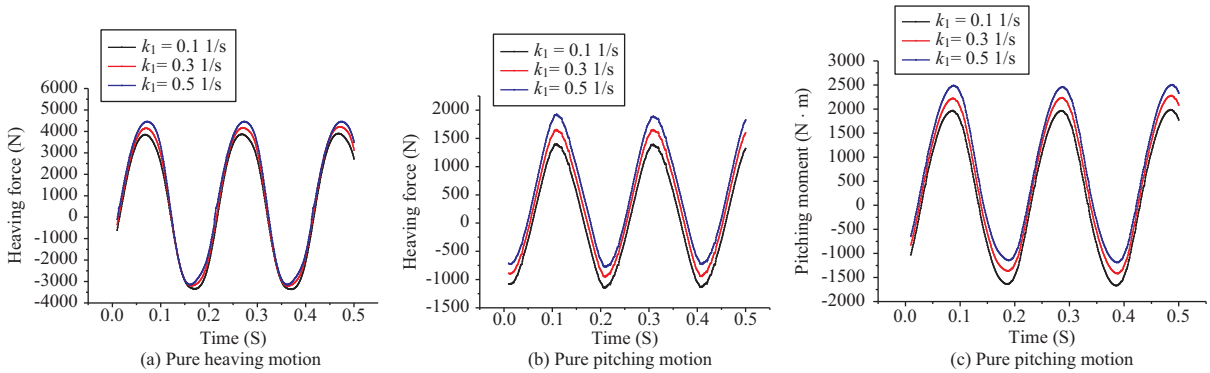

Fig. 18. Variations of heaving force and pitching moment with k_1 in time history.

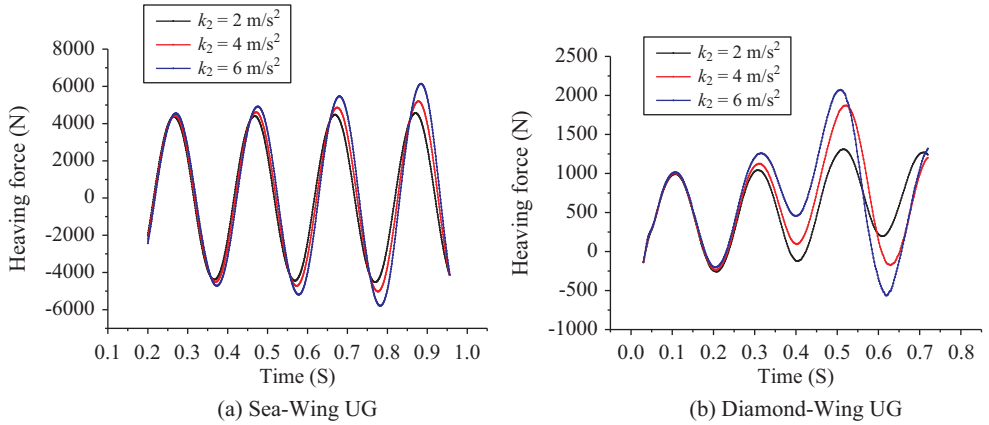

Fig. 19. Variations of heaving force with respect to k_2 and time during the UG's pure motion in heave, motion frequency, f=5Hz.

in an unsteady and a nonuniform flow field is discussed in this section. The initial condition of nonuniform unsteady flow and forced UG in pure heave motion and in pure pitch motion are those in Case 3 and Case 4 given in Table 6. The initial unsteady flow field was formulated and generated using the UDF in the STAR-CCM+ solver as follows:

$$U_2 = U_0 + k_2 \times t\,, \tag{18}$$

where U_2 is the velocity of unsteady flow; U_0 is the initial speed (= 2.0 m/s); k_2 denotes the acceleration of unsteady flow in surge, i.e., 2.0 ,4.0, and 6.0 m/s^2 ; t denotes the time step.

1) Pure Heaving Motion Simulation

To analyze the effect of the acceleration of unsteady flow on the hydrodynamic performance of the Diamond-Wing UG in heaving motion, the initial condition and forced motion state of Case 4 in Table 6 were set using the UDF according to Eq. (13). The circular frequency of heaving motion ω was set as a constant value and $\omega = 10\pi$. The unsteady inlet velocity was set using the UDF according to Eq. (16), and k_2 = 2.0, 4.0, and 6.0 m/s^2.

Fig. 19 shows that the heaving force value of the UGs periodically changed, and the peak value increased with the increase of the inflow coefficient k_2. For the Diamond-Wing UG, the heaving force is small compared with the conventional UG at the initial point, but the response to the acceleration of unsteady flow in surge is relatively significant, i.e., the heaving force increases obviously with the increases in k_2.

The peak difference comparison results are as follows. The peak value of the Diamond-Wing UG is lower than that of the conventional Sea-Wing UG and the differences are in the range 70%-76%, as shown in Table 7, owing to the special structure of the diamond wing.

To study the effect of the UG's heaving motion frequency on the heave force in unsteady flow, the UG's motion state was set using the UDF according to Eq. (15). The circular frequencies of heaving motion ω were set as 8π, 10π, and 12π; and the motion frequencies f in heave were 4 Hz, 5 Hz, and 6 Hz, respectively. The unsteady inlet velocity was set using the UDF according to Eq. (18) and k_2 = 2.0 and 6.0 m/s^2 in this case study. Fig. 20 shows that changes in the heaving motion frequency of the UG resulted in larger oscillations of the heaving force on the UG over time, the peak of the heaving force is advanced, and the peak value improves with increases in motion frequency f during the heaving.

2) Pure Pitching Motion Simulation

To analyze the effect of the acceleration of unsteady flow on

Table 7. Comparison of heaving force difference of two types UGs in k_2 = 2 m/s^2, f = 5 Hz.

Peak value	Sea-Wing UG (N)	Diamond-Wing UG (N)	Difference (N)	Percentage Difference
1st	4363.815	1043.040	-3320.775	-76.10%
2nd	4402.752	1311.589	-3091.163	-70.21%
3rd	4576.835	1270.087	-3306.748	-72.25%

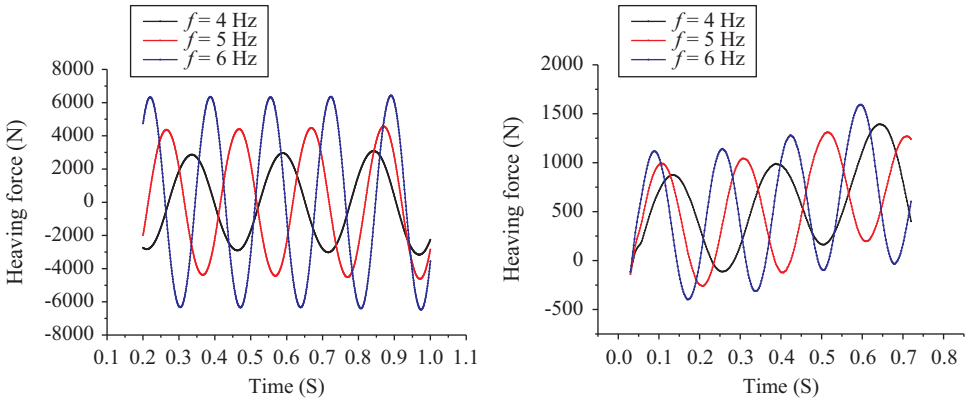

(a) Conventional UG, k_2 = 2.0 m/s^2 (b) Diamond-Wing UG, k_2 = 2.0 m/s^2

Fig. 20. Variation of heaving force versus pure heave motion frequency f in time history.

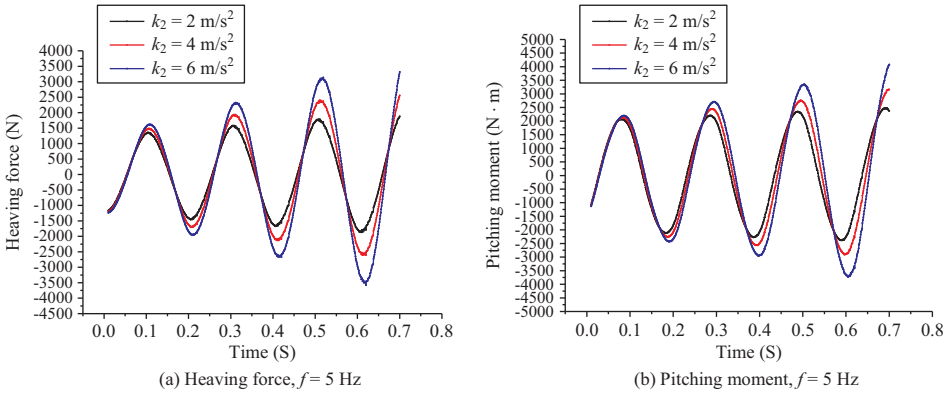

(a) Heaving force, f = 5 Hz (b) Pitching moment, f = 5 Hz

Fig. 21. Variations of the Conventional Sea-Wing UG heaving force and pitching moment with k_2 at pure pitch motion frequencies f = 5 Hz in time history.

the hydrodynamic performance of the Diamond-Wing UG motion in pitch, the forced UG motion state shown in Case 4 in Table 6 was set using the UDF according to Eq. (16). The circular frequencies of heaving motion ω were set to 8π, 10π, and 12π; and the frequencies of heaving motion f were 4 Hz, 5 Hz, and 6 Hz, respectively. The unsteady inlet velocity was set using the UDF according to Eq. (18), and k_2 = 2.0, 4.0, and 6.0 m/s^2. Figs. 21(a)-(f) show the variation tendency of the heaving force and pitching moment for the Diamond-Wing UG to perform pitching motions with different motion frequencies. These results show that the peak value of the heaving force increases with increases in the acceleration of unsteady flow k_2. With increases in pitching frequency, the peak values of both the heaving force and pitching moment increase. Fig. 21 shows that the heaving force and pitching moment of the conventional UG are all larger than that of the Diamond-Wing UG.

To study the effect of the pitching motion frequency on the heaving force and pitching moment in unsteady flow, the UG motion state was set using the UDF according to Eq. (16). The circular frequencies of heaving motion ω were set at 8π, 10π and 12π; and the frequencies of heaving motion f were 4 Hz, 5 Hz, and 6 Hz, respectively. The unsteady inlet velocity was set using the UDF according to Eq. (18) and k_2 = 2.0, 4.0, and 6.0 m/s^2 in this case study.

The comparisons of the simulation results of UGs using conventional wing with the diamond wing in the case k_2 = 2.0 m/s^2 are shown in Figs. 23(a) and (b) and Figs. 24(a) and (b). Figs. 23(a) and (b) show the variations of heaving force and pitching moment of the conventional Sea-Wing UG in time history, and Figs. 24(a) and (b) show that of Diamond-Wing UG

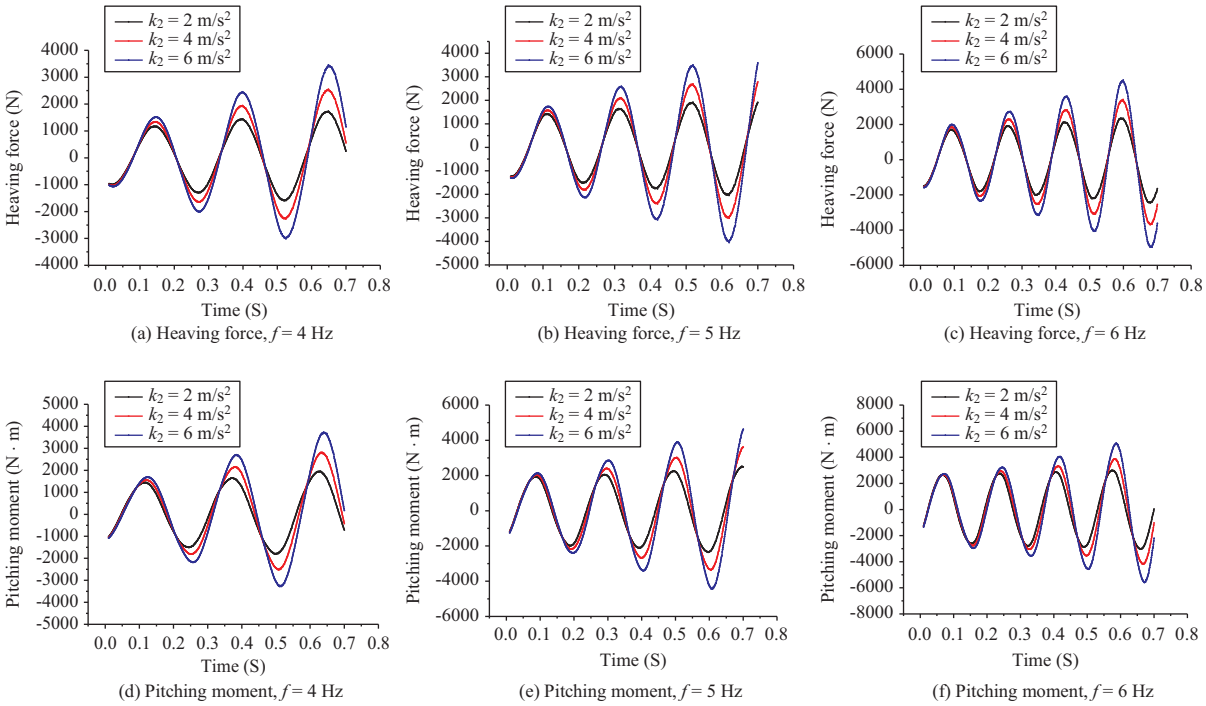

Fig. 22. Variations of the Diamond-Wing UG heaving force and pitching moment with k_2 at pure pitch motion frequencies f = 4, 5, and 6 Hz in time history.

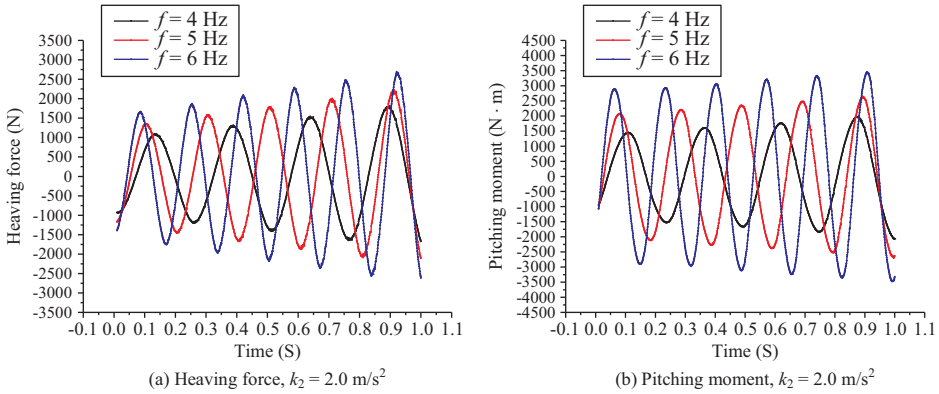

Fig. 23. Variations of heaving forces and pitching moments of conventional Sea-Wing UG with pure motion frequency in pitch for k_2 = 2.0 m/s^2 in time history.

in time history. Obviously, the heaving force and pitching moment of the conventional UG are all larger than that of Diamond-Wing UG. In summary, the difference comparison results of the UGs unsteady motion in heave and pitch as shown in Figs. 23(a) and (b) and Figs. 24(a) and (b) are shown in Tables 8 and 9. The peak values of the Diamond-Wing UG oscillation motion in pitch and heave are lower than those of the conventional Sea-Wing UG and the difference is kept within 10% for the case k_2 = 2.0 m/s^2.

Figs. 24(a)-(f) show that the heaving force changes to larger values with the increase in time because the inlet velocity increases in an unsteady flow field. When the motion frequency of the UG in heave varies, the peak of the heaving force appears in advance and the peak value is improved with the increasing frequency in heaving motion for all accelerations of unsteady flow k^2. This phenomenon is the same as that occurring during the heaving motion in an unsteady flow field.

In the case study with a variable nonuniform flow coefficient, the time-varying results show that the proposed UG motion in heave and pitch maintains a small increase in the peak value of the heaving force and the pitching moment in the time history. The time-varying results of the case study involving a variable unsteady acceleration flow coefficient show that the proposed UG could offer improved controllability and anti-flow ability.

VI. CONCLUSIONS

In this study, a proposed UG with a diamond-shaped wing was developed and analyzed. In addition, a relatively accurate numerical analysis procedure was successfully developed by

Table 8. Comparison of heaving force difference of two types UGs in k_2 = 2.0 m/s^2, f = 5 Hz.

Peak value	Conventional UG (N)	Diamond-Wing UG (N)	Difference (N)	Percentage Difference
1st	1285.882	1170.645	-115.237	-8.96%
2nd	1567.809	1446.947	-120.862	-7.71%
3rd	1771.570	1732.502	-39.067	-2.21%

Table 9. Comparison of pitching moment difference of two types UGs in k_2 = 2.0 m/s^2, f = 5 Hz.

Peak value	Conventional UG (N-m)	Diamond-Wing UG (N-m)	Difference (N-m)	Percentage Difference
1st	2068.955	1932.091	-136.864	-6.62%
2nd	2203.950	2045.380	-158.570	-7.19%
3rd	2347.097	2262.419	-84.678	-3.61%

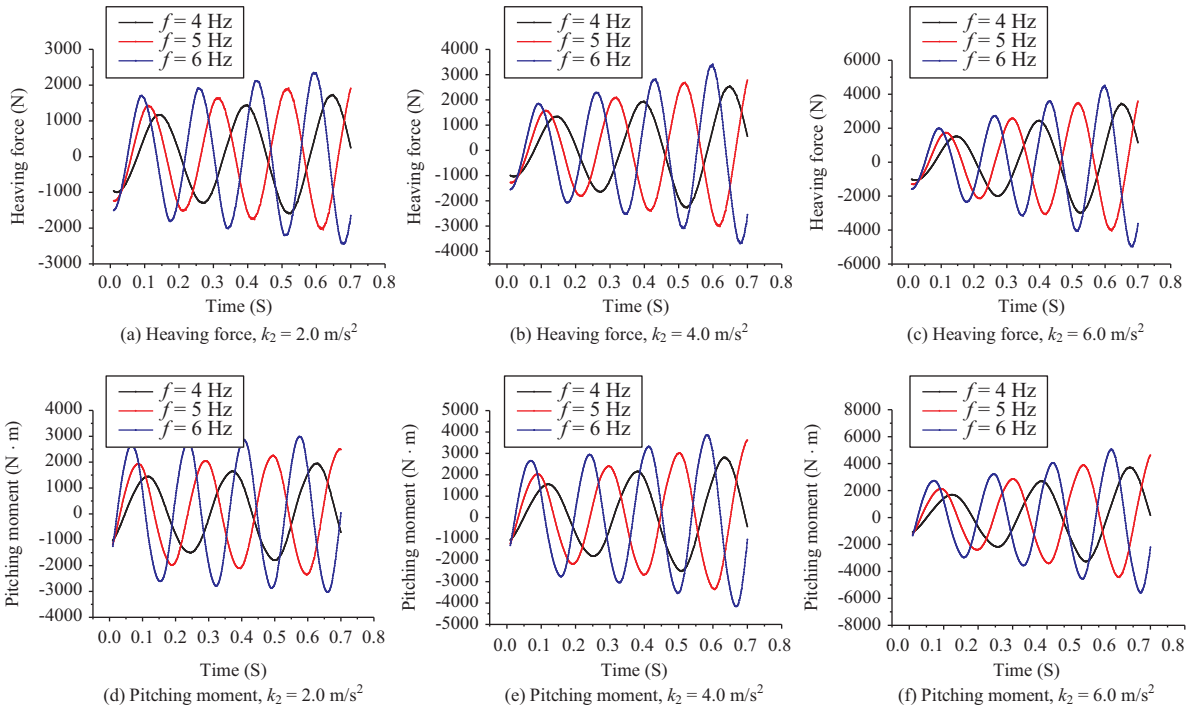

Fig. 24. Variations of heaving forces and pitching moments with pure motion frequency for k_2 = 2.0, 4.0, and 6.0 m/s^2 in pitch in time history.

applying RANS solvers using CFD methods; this procedure is a powerful tool to analyze the hydrodynamic performance of integrated UG hull-wing-tail bodies operating in various unsteady and nonuniform inflows and motion attitudes. The findings of this study are of practical importance for estimating the body hull efficiency, lift-to-drag ratio of the wing, and hydrodynamic pitching moment and heaving force applied to the wing-body UGs. The proposed new diamond-shaped wing of the UG has two important merits. In comparison with the traditional UG with a backswept wing (Sea-Wing UG), the lift-to-drag ratio of the diamond-shaped wing was increased by 6.5% to 14% for AOAs in the range 4°-12°, and the hull efficiency increased by 27% to 45% as well for AOAs in the range 2°-18°. After optimization of the diamond-shaped wing, the optimal value of the tilt angle selected was in the range 15°-20°, and a remarkable increase in the hull efficiency of the UG was attained. This phenomenon is mainly due to the influence of the elevation difference in the two sets of wings in the diamond-shaped wing arrangement on the in-between flow to the rear set of wings.

Based on the optimized wing-body UG configuration (tilt angle of 15°), unsteady RANS studies on the hydrodynamic performance of the Diamond-Wing UG were carried out. In the validation study during the unsteady RANS calculation, an ellipsoid with a slenderness ratio of 6:1 was selected to calculate the hydromantic derivatives. The validation results show that the errors between the numerical and theoretical values are within the tolerance limits.

The quantitative and qualitative effects of nonuniform and unsteady currents on the UG's harmonically forced motion performance were studied in four cases studies. In Case 3, the dis-

advantages of using the conventional wing in nonuniform unsteady flow were experienced owing to the obvious hydrodynamic heaving force acting on the conventional wing being larger than that on the diamond wing. In Case 4, comparisons of pure pitching motion simulation of the two types of UGs showed that the peak values of pitching moment in time history are lower than those of the conventional Sea-Wing UG and the difference is kept within 10% in unsteady acceleration flow conditions with $k_2 = 2.0$ m/s^2. In conclusion, the simulation results showed that the UG with the proposed diamond-shaped wing possesses anti-flow ability and strong maneuverability in nonuniform and unsteady inflow conditions.

In future work, the relationship between the nonuniform flow parameter k_1 and unsteady acceleration flow k_2 will be established with real-time long-term collection of oceanic data. The hydrodynamic performance of UGs mounted with hybrid propulsion, e.g., propellers and buoyancy engines, will also be studied for enhancements in maneuverability and speed.

ACKNOWLEDGEMENTS

We would like to thank the National Natural Science Foundation of China (No. 51409230) and Zhejiang Zhoushan Science and Technology Project (No. 2018C81041) and the National Key Special Research Plan of China Ministry of Education (No. 2017YFC0306100) for their financial support. In addition, we would like to thank Professor W. H. Wang at Zhejiang University and Taiwan Ocean University and the anonymous reviewers whose comments were helpful in improving the original manuscript.

REFERENCES

Bettle M. C., A. G. Gerber and G. D. Watt (2009). Unsteady analysis of the six DOF motion of a buoyantly rising submarine, Computers and Fluids 38 (9), 1833-1849.

Bettle M. C., A. G. Gerber and G. D. Watt (2014). Using reduced hydrodynamic models to accelerate the predictor-corrector convergence of implicit 6-DOF URANS submarine maneuvering simulations, Computers and Fluids 102, 215-236.

Chen, C. W., J. S. Kouh and J. F. Tsai (2013a). Modeling and simulation of an AUV simulator with Guidance System. IEEE Journal of Oceanic Engineering 38 (2), 211-225.

Chen, C. W., J. S. Kouh and J. F. Tsai (2013b). Maneuvering modeling and simulation of AUV dynamic systems with euler-rodriguez quaternion method. China Ocean Engineering 27 (3), 403-416.

Chen, C. W., Y. Jiang, H. C. Huang, D. X. Ji, G. Q. Sun, Z. Yu and Y. Chen (2017). Computational fluid dynamics study of the motion stability of an autonomous underwater helicopter. Ocean Engineering 143, 227-239.

Graver, J. G. and N. E. Leonard (2001). Underwater glider dynamics and control. Proc.int. symposium on Unmanned Untethered Submersible Tech.

Holloway, A. G. L., T. L. Jeans and G. D. Watt (2015). Flow separation from submarine shaped bodies of revolution in steady turning. Ocean Engineering 108, 426-438.

Huang, K. L, Y. J. Pang, Y. M. Su and J. Zhu (2008). Research on calculation method of linear hydrodynamic coefficients of submersibles. Journal of Ship Mechanics 2008(05), 697-703.

Jeans, T. L. and A. G. L. Holloway (2010). Flow separation lines on axisymmetric bodies with tapered tails. J. Aircr. 47(6).

Kannappa, P. P., Y. Singh and V. G. Idichandy (2015). Numerical study of a twin sphere pressure hull and outer fairing for manned submersible. Underwater Technology. IEEE 2015, 1-11.

Liu, Y., Q. Shen, D. L. Ma and X. J. Yuan (2016). Theoretical and experimental study of anti-helical motion for underwater glider. Applied Ocean Research 60, 121-140.

Sakthivel, R., S. Vengadesan and S. K. Bhattacharyya (2011). Application of non-linear k-e turbulence model in flow simulation over underwater axisymmetric hull at higher angle of attack. Journal of Naval Architecture & Marine Engineering 8(2), 149-163.

Ting, M. C., M. A. Mujeebu and M. Z. Abdullah (2012). Numerical study on hydrodynamic performance of shallow underwater glider platform. Indian Journal of Geo-Marine Sciences 41(2), 124-133.

Wang, S. X., X. J. Sun, Y. H. Wang, J. G. Wu and X.M. Wang (2011). Dynamic modeling and motion simulation for a winged hybrid-driven underwater glider. China Ocean Engineering 25(1), 97-112.

Wu, J., C. Chen and S. Wang (2010). Hydrodynamic effects of a shroud design for a hybrid-driven underwater glider. Sea Technology 51(6), 45-47.

Wu, L. H., J. C. Yu and X. S. Feng (2006). Hydrodynamic research and motion analysis of AUG. Ship Engineering (1), 12-16.

Wu, F. L., X. G. Wu, J. Xu, Y. Y. Ma and H. B. He (2009). Method of numerical calculation of the 3D viscous flow field over a submarine main hull. Shipbuilding of China 50(02), 12-22.

Yang, L. H. (2009). Research on numerical calculation method of maneuvering hydrodynamic derivatives of submarines with external loading. Ph.D. Thesis, Harbin Engineering University. Unpublished. (in Chinese)

Yang, C. J., S. L. Peng, S. Fan, S. S. Fan, S. Y. Zhang, P. F. Wang and Y. Chen (2016). Study on docking guidance algorithm for hybrid underwater glider in currents. Ocean Engineering 125, 170-181.

Yu, J. C., A. Q. Zhang, W. M. Jin, Q. Chen, Y. Tian and C. J. Liu (2011). Development and experiments of the sea-wing underwater glider. China Ocean Engineering (04), 721-736.

Yu, J., F. Zhang, A. Zhang, W. Jin and Y. Tian (2013). Motion parameter optimization and sensor scheduling for the sea-wing underwater glider. IEEE Journal of Oceanic Engineering 38(2), 243-254.

Yu, X. Z. (2012). Hydrodynamic Performance Analysis of the Mini-Underwater Vehicle and interaction between two bodies. Ph. D Thesis, Department of Naval Architecture and Ocean Engineering, Harbin Engineering University, unpublished. (in Chinese).

Zhang, W. X. (2016). Small amplitude PMM numerical simulation of ellipsoids. Pioneering Science, 29(12), 137-138.

Zhang, X. P. (2008). Research on Maneuverability and Motion Simulation of Multifunctional Submersible. Ph.D. Thesis, Harbin Engineering University, unpublished. (in Chinese)